scientific reports

Check for updates

OPEN

Mechanistic studies of Ca^{2+}-induced classical pyroptosis pathway promoting renal adhesion on calcium oxalate kidney stone formation

Jinjie Xiang, Maoxin Lv, Yuhui Luo, Kunbin Ke, Baiyu Zhang, Mengyue Wang, Kun Zhang & Hao Li✉

This study aims to investigate the role of hypercalciuria and pyroptosis in the formation of calcium oxalate kidney stones. Bioinformatics analysis was performed to compare the correlation of pyroptosis scores and cell adhesion scores between Randall's plaques and normal tissues from kidney stone patients. For the in vitro experiments, we investigated the effects of high concentrations of Ca^{2+} on the pyroptosis and adhesion levels of renal tubular epithelial cells and examined the adhesion levels and crystal aggregation of the cells in high Ca^{2+} concentrations environment by knockdown and overexpression of the key pyroptosis gene, GSDMD, and we verified the effects of Ca^{2+} concentration on pyroptosis and adhesion levels, kidney injury, and crystal deposition by in vivo experiments. Bioinformatic results showed that the scores of pyroptosis and cell adhesion in Randall's plaques of patients with kidney stones were significantly higher than those in normal tissues, and pyroptosis was highly positively correlated with cell adhesion. In vitro and in vivo experiments showed that high concentrations of Ca^{2+} activated the NLRP3/Caspase-1/GSDMD pathway of pyroptosis through ROS and up-regulated the expression of adhesion-related proteins, and GSDMD could regulate the adhesion level of renal tubular epithelial cells by mediating the level of pyroptosis, thereby affecting the adhesion and deposition of calcium oxalate crystals. Our findings reveal that the Ca^{2+}-induced classical pyroptosis pathway may be a potential mechanism to promote calcium oxalate kidney stone formation, which provides new insights into the etiology of kidney stones.

Keywords Pyroptosis, Cell adhesion, Hypercalciuria, Reactive oxygen species, Kidney stones

Kidney stones are a urologic disease with relatively high incidence and recurrence rates worldwide, with prevalence rates of 7–14%, 5–9%, and 1–5% in North America, Europe, and Asia, respectively[1]. The majority of kidney stones are calcium oxalate (CaOx) stones[2]. The renal tubules are the main kidney components injured by stone obstruction and calcium oxalate[3,4]. The main process of renal stone formation is urine supersaturation, crystal nucleation, and migration to the surface of renal tubular epithelial cells (RTECs)[5], and the deposition of crystals in the kidneys leads to oxidative stress and upregulates the expression of inflammatory factors[6], which promotes RTECs damage. The membrane structures of the injured RTECs such as microvilli and tight junctions will be disrupted, thereby increasing cell adhesion to crystals, and the adhesion is critical for the nucleation and growth of stones[7].

Randall's plaque is considered the precalculus lesion to renal calculi, and the precalculus lesions were classified into Randall's plaque and Randall's plugs, termed Randall's plaque type I and II[8]. Randall's plaques play an important role and are a prerequisite for calcium oxalate stone formation and growth in idiopathic calcium oxalate stone formers, and approximately 75% of calcium oxalate stones are formed attached to sites of Randall's plaques[9,10].

Pyroptosis is a newly discovered type of programmed cell death and natural immune response of the body[11,12], which is widely involved in the development and regulation of many diseases, such as metabolic diseases[13,14],

Department of Urology, First Affiliated Hospital of Kunming Medical University, Kunming 650032, China. ✉email: lihao834@sina.com

renal fibrosis[15,16], and the development and metastasis of many tumors[17,18]. Kidney stones are also one of the metabolic diseases and its pathogenesis is still unclear. It has shown that molecules of the classical pyroptosis pathway are related to the formation of kidney stones[19,20]. RTECs could undergo oxidative stress injury in the environment of CaOx crystals, leading to the activation of NLRP3 inflammasome and the production of inflammatory factors through pyroptosis[21,22], while inhibiting NLRP3 expression can reduce the pyroptosis level of RTECs and alleviate the damage caused by CaOx crystal deposition in kidney tissue[23]. In addition, vitexin could down-regulate the expression of pyroptosis-related proteins, and inhibit the apoptosis of RTECs and the expression of adhesion-related proteins in kidney stone model mice, indicating that inhibition of pyroptosis has a protective effect on kidney stones[24].

The most common metabolic abnormality in patients with kidney stones is hypercalciuria, which accounts for approximately 40–60% of kidney stone cases[25,26]. Hypercalciuria can induce crystal formation in the renal tubule lumen, leading to supersaturation, precipitation, tubular obstruction, cellular damage, and a significant increase in the risk of kidney stones[27]. Most of the previous studies demonstrated the effects of oxalate and CaOx on pyroptosis. This study is the first to investigate the mechanism of pyroptosis triggered by elevated Ca^{2+} on kidney stone formation. Moreover, the 24-hour urinary Ca^{2+} concentration of patients with recurrent stones was nearly 50% higher than that of the nonrecurrent group, which suggests that hypercalciuria is also a major predictor of kidney stone recurrence[28]. Therefore, exploring the potential relationship between Ca^{2+}-induced pyroptosis and crystal adhesion will not only provide new insights and targets for the pathogenesis of kidney stones, but also be of great significance for the prevention of clinical kidney stone recurrence.

Results

Identification of DEGs and enrichment analysis

We screened a total of 525 differentially expressed genes (DEGs), which are shown in the volcano plot and heatmap (Fig. 1a, b). The DEGs identified in GSE73680 contained 297 upregulated genes and 228 downregulated genes based on $|\log2FC| > 0.5$ and $p < 0.05$. Then, Gene Ontology (GO) enrichment analysis was performed on the upregulated and downregulated genes (Fig. 1c), and the enriched functions included nephron tubular epithelial cell differentiation, mesenchymal cell differentiation, metanephric collecting duct development, mesenchyme development, and cell differentiation involved in kidney development. The enrichment results were visualized with a cnetplot (Fig. 1d, e), where each node represents a gene, and each edge represents an interaction between two genes. Cnetplots are used to accurately determine key signaling pathways and their

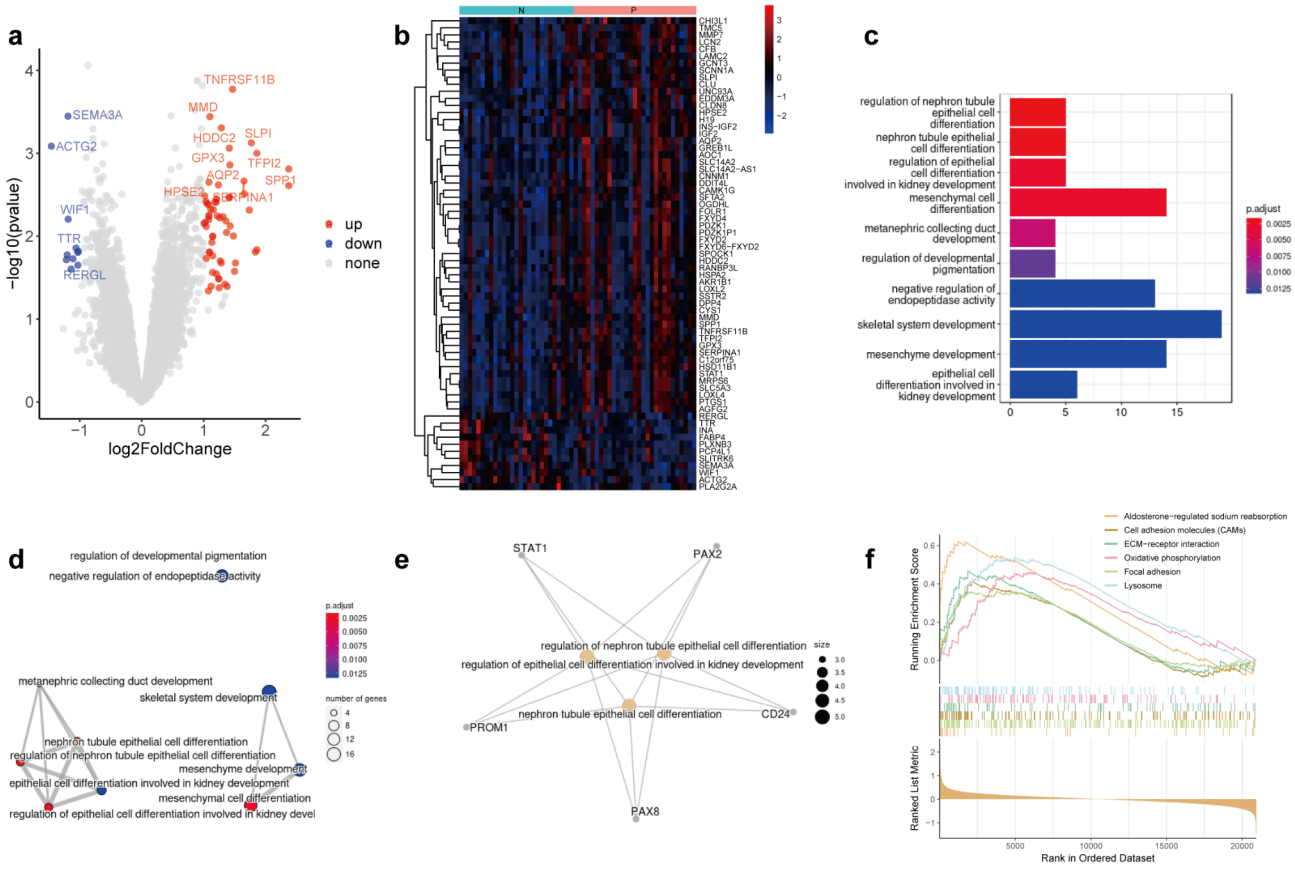

Fig. 1. (**a**) Volcano plot and (**b**) heatmap of differentially expressed genes between the Randall plaque tissues of CaOx stone formers and normal tissues of CaOx stone patients (group P vs. group N). (**c**-**e**) GO enrichment analysis. (**f**) Enrichment analysis of the KEGG pathway.

upstream and downstream genes. In the lower-left corner of the figure, the genes involved in the differentiation of renal epithelial cells are interconnected. The graph links genes and biological concepts (such as GO terms or Kyoto Encyclopedia of Genes and Genomes [KEGG] pathways) into a network for viewing important genes involved in multiple enriched pathways that possibly belong to multiple annotation categories. The results demonstrated the top three functions with the most significant *p*-value: regulation of nephron tubular epithelial cell differentiation, regulation of epithelial cell differentiation involved in kidney development and nephron tubular epithelial cell differentiation, as well as the core genes that regulate these functions: STAT1, PAX2, PAX8, PROM1 and CD24 (Fig. 1e). The results of KEGG pathway enrichment analysis showed that cell adhesion, lysosomal, and oxidative phosphorylation pathways that may be associated with cell death were active in the kidney stone group (Fig. 1f).

WGCNA of coexpression modules related to pyroptosis and cell adhesion

The results of sample clustering showed that there were no outliers. To ensure that the interaction between genes conforms to a scale-free distribution to the greatest extent, we first determined the soft threshold of the data and generally chose the lowest soft power threshold with a scale-free topology Model Fit greater than or equal to 0.8. Here, we chose 8 as the soft threshold for the subsequent analysis (Fig. 2a). A total of 21 modules were clustered by constructing the coexpression network (Fig. 2b). After determining the existence of 21 coexpression modules in the gene expression data, we used the sample grouping information as a phenotype to analyze the correlation between each module and the N, C, and P groups. Red represents a positive correlation between the expression module and grouping, while blue represents a negative correlation (Fig. 2c). For example, the MEred module was positively correlated with group P, with a correlation of 0.29, $p < 0.05$.

The Ca^{2+} pathway plays an important role in kidney stones. We performed enrichment analysis on the screened modules, and the results showed that the turquoise module contained the largest number of Ca^{2+} pathway-related genes (Fig. 2d). Therefore, we screened the turquoise module as a key module associated with kidney stones. The results of single-sample enrichment analysis showed that the MEBlue, MEroyalblue, MEred, and MEblack modules were positively correlated with pyroptosis (Fig. 2e). Combined with the above analysis, the MEBlue, MEroyalblue, MEred, MEblack, and turquoise modules were selected as the key modules associated with pyroptosis and the Ca^{2+} pathway in kidney stone development. We further looked at the hub core genes that appeared in the pyroptosis gene set in these four modules and mapped the network using Cytoscape (Fig. 2f–i), where the labeled pyroptosis-related genes are in the center of the network, including MUC20, MST1, SLA16A4, VDR, and HKDC1 in the red module, which are related to epithelial cell differentiation (Fig. 2f). The MEblack module was associated with immune regulation and included NLRP7, IL-32, and PRF1 (Fig. 2h). The MEred module was most closely related to renal tubular epithelial cells, and we examined the coexpression network of genes in this module that were regulated by genes related to cell adhesion, among which the hub genes were MUC1, EPCAM1, CCN3, and ATP1B1 (Fig. 2g). In the gene coexpression network of the turquoise module, although a small number of pyroptosis-related genes were involved in this module, the classical pyroptosis gene gasderminD (GSDMD) was included (Fig. 2i). Subsequently, we found that the genes interacting with GSDMD included NLRP3, cysteinyl aspartate specific proteinase-1 (Caspase-1), GSDMD, IL-1β, and IL-18 through STRING protein interaction analysis (Fig. 2j).

Functional enrichment analysis of key pyroptosis modules

GO enrichment analysis was used to identify the biological functions of the above MEblue, MEroyalblue, MEred, and MEblack modules. The results showed that the MEblue module was related to the regulation of mRNA catabolic processes (Supplementary Fig. 1a), the MEroyalblue module was associated with RNA variable shearing (Supplementary Fig. 1b), the final MEred module was related to the regulation of renal tubular development and differentiation of renal tubular epithelial cells (Supplementary Fig. 1c), and the MEblack module was associated with the immunomodulation of lymphocyte-mediated immunity, activation of signal transduction by immune response, complement activation, B-cell-mediated immunity, immunoglobulin-mediated immune response, and humoral immune response (Supplementary Fig. 1d).

Differential expression analysis of modular genes and scoring for pyroptosis and cell adhesion

We compared the expression levels of the core pyroptosis- and cell adhesion-related genes in the modules of groups P and N. In the MEblue module, the expression levels of the pyroptosis-related genes ANXA2 and CHMP4A were upregulated in group P, while ASIC1 was downregulated in group P (Fig. 3a). The pyroptosis-related genes HKDC1, MST1, SLC16A4, and VDR and the cell adhesion-related gene MUC1 were highly expressed in group P in the MEred module (Fig. 3b, c). However, the pyroptosis-related genes in the MEblack module showed no significant difference between groups P and N (Fig. 3d). The MEred module, which was the most relevant to the function of epithelial cells, was used to identify the core pyroptosis-related genes SLC16A4, HKDC1, VDR, MST1, and MUC20 and the core cell adhesion-related genes MUC1, ATP1B1, CCN3, and EPCAM and to single-sample gene set enrichment analysis (GSEA) was used to score the samples of the P and N groups. The results showed that the pyroptosis and cell adhesion scores of group P were significantly higher than those of group N (Fig. 3e, f). Finally, we analyzed the correlation between the pyroptosis score and cell adhesion score, and the results showed that pyroptosis was highly and positively correlated with cell adhesion (Fig. 3g, $R = 0.91$).

High Ca^{2+} promoted renal tubular epithelial cell injury

The CCK-8 results showed a gradual decrease in cell viability with increasing concentrations of Ca^{2+}, and the lactate dehydrogenase (LDH) assay results showed that the level of LDH released from the cells and the degree

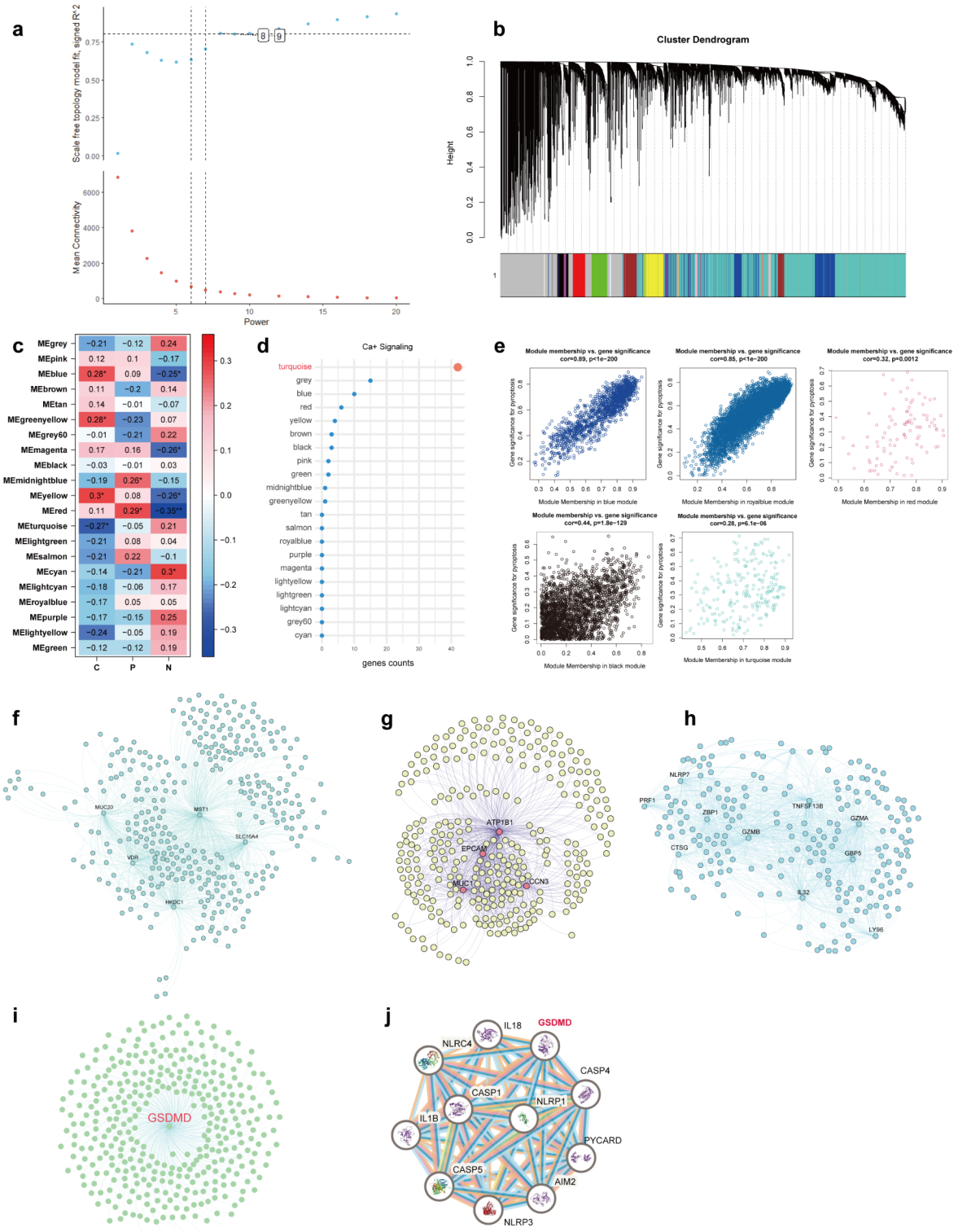

Fig. 2. WGCNA of coexpression modules related to pyroptosis and cell adhesion. (**a**) Determination of soft threshold. (**b–c**) Dendrogram of cluster modules. (group P: Randall's plaque tissues from CaOx stone formers, group N: normal tissues from CaOx stone patients, and group C: healthy controls). (**d**) Ca^{2+} pathway enrichment analysis. (**e**) Heatmap of correlation between coexpression modules and different samples. Coexpression network of genes related to (**f**) pyroptosis and (**g**) cell adhesion in the MEred module. (**h**) Coexpression network of pyroptosis-related genes in the MEblack module. (**i**)Coexpression network of GSDMD. (**j**) Interaction analysis of GSDMD.

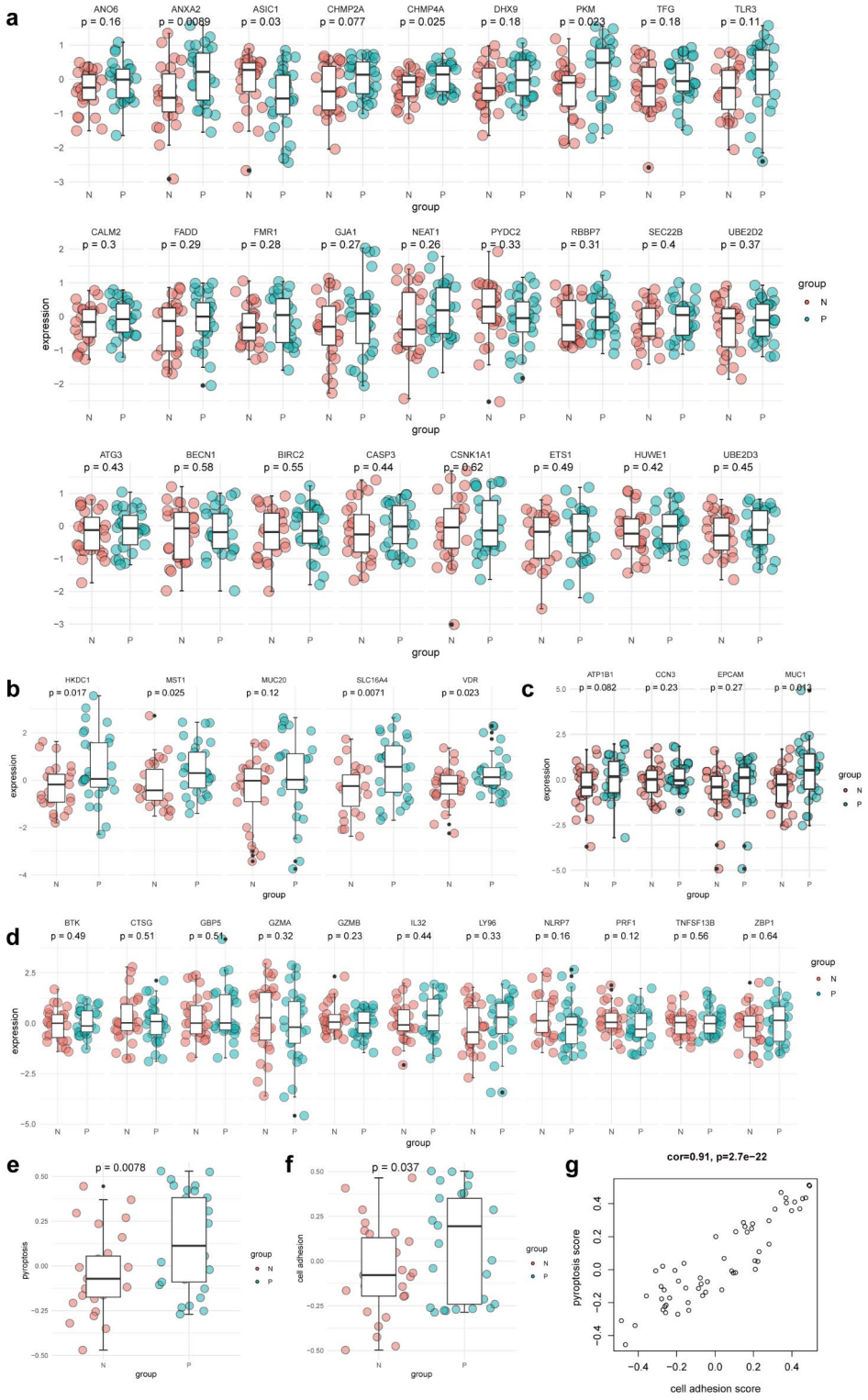

Fig. 3. Expression levels of core pyroptosis-related genes in the (**a**) MEblue and (**d**) MEblack modules, expression levels of core (**b**) pyroptosis- and (**c**) cell adhesion-related genes in the MEred module, and scores of (**e**) pyroptosis and (**f**) cell adhesion in group P and N (group P: Randall's plaque tissues from CaOx stone formers, and group N: normal tissues from CaOx stone patients). (**g**) Correlation between pyroptosis score and cell adhesion score.

of cell damage increased as the concentration of Ca^{2+} increased. Cell viability was significantly decreased when the concentration of Ca^{2+} reached 10 mM (Fig. 4a), while LDH release was significantly increased when the concentration of Ca^{2+} reached 20 mM compared to the control treatment (Fig. 4b). According to the above experimental results, we used 10 mM Ca^{2+} for subsequent experiments.

It has been shown that 5 mM Ca^{2+} is the normal physiological level to which renal tubular epithelial cells may be exposed[27]. ELISA (Fig. 4c) and Western Blot (Fig. 4d) results also showed that the expression levels of the pyroptosis-related proteins NLRP3, Caspase-1/p20, GSDMD, GSDMD-N, IL-1β, IL-18, and the adhesion-related proteins osteopontin (OPN), CD44, monocyte chemotactic protein-1 (MCP-1), and integrin beta 1 (ITGB1) were not significantly different in the HK-2 cells compared with the Control group after treatment with 5 mM of Ca^{2+} for 24 h, 48 h, and 72 h, so we used 5 mM as a control for subsequent experiments. In addition, 20 mM Ca^{2+} was used to confirm the effect of a high Ca^{2+} concentration on cell damage in a concentration-dependent manner.

High Ca^{2+} promoted pyroptosis and adhesion changes in HK-2 cells

Pyroptosis-related microstructural changes in Ca^{2+}-treated HK-2 cells

The transmission electron microscopy results showed that HK-2 cells in the control group had normal morphology and intact cell membranes. Compared with the 5 mM Ca^{2+} group, the cells in the group treated with a high concentration of Ca^{2+} showed obvious pyroptosis-related microstructural changes such as abnormal cell morphology, local damage to the cell membrane, cell-matrix overflow, free organelles in some areas and many vacuoles (Fig. 5a), and the above situation was more severe in the 20 mM Ca^{2+} group than in the 10 mM group.

Ca^{2+} treatment increased the expression levels of pyroptosis and adhesion-related proteins

The Western blot (Fig. 5b) and ELISA (Fig. 5c) results showed that the expression levels of pyroptosis-related proteins NLRP3, Caspase-1/p20, GSDMD, GSDMD-N, IL-1β, and IL-18 and adhesion-related proteins OPN, CD44, MCP-1, and ITGB1 were significantly increased in HK-2 cells treated with Ca^{2+} (10 mM and 20 mM [$n = 3$]), and the effect of Ca^{2+} on the expression levels of these proteins was concentration- and time-dependent.

GSDMD expression regulated pyroptosis in HK-2 cells

We regulated the pyroptosis level of HK-2 cells by knocking down and overexpressing GSDMD, a key gene in the classical pyroptosis pathway. The qPCR results showed that the mRNA expression levels of the pyroptosis-related genes GSDMD, IL-1β, and IL-18 were significantly downregulated and upregulated with GSDMD knockdown and overexpression after 10 mM Ca^{2+} treatment for 24 h, 48 h, and 72 h, respectively (Supplementary Fig. 2a). However, the mRNA expression levels of NLRP3 and Caspase-1 were not affected by changes in the expression levels of GSDMD (Supplementary Fig. 2a). In addition, similar results were demonstrated by Western blot (Supplementary Fig. 2b) and ELISA (Supplementary Fig. 2c).

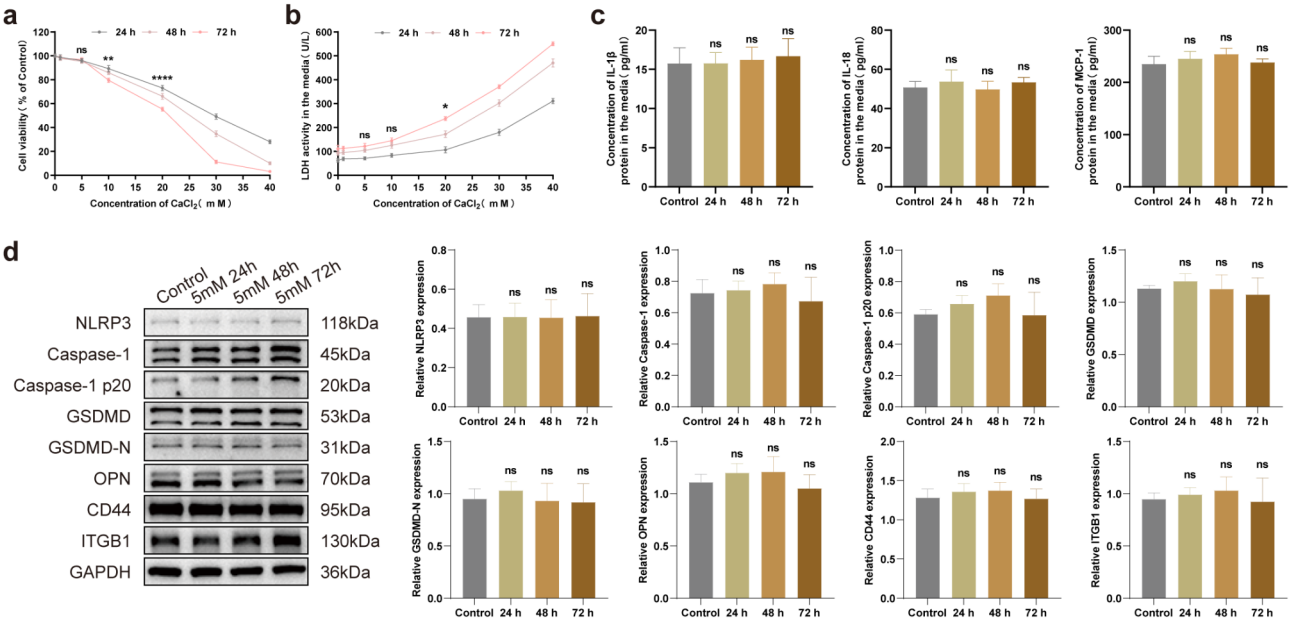

Fig. 4. In vitro: Ca^{2+} promotes renal tubular epithelial cell injury in a concentration- and time-dependent manner. Cell viability (**a**) and LDH activity in the media (**b**). Pyroptosis- and adhesion-related protein expression in the HK-2 cells using ELISA (**c**) and Western Blot images and their graphical quantification (**d**). $^{*}p < 0.05$; $^{**}p < 0.01$; $^{****}p < 0.0001$.

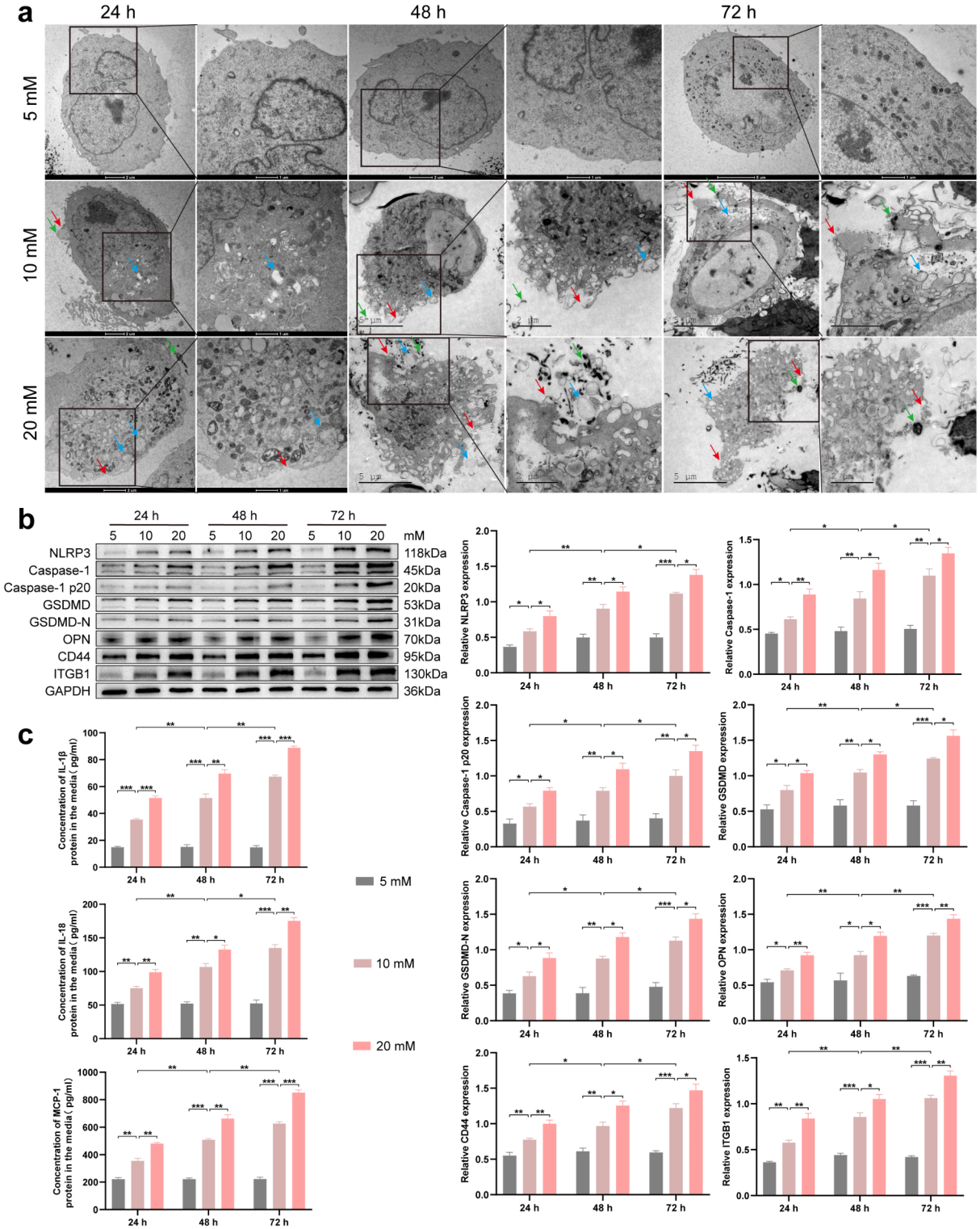

Fig. 5. In vitro: High Ca^{2+} upregulates the expression of pyroptosis- and adhesion-related proteins in a concentration- and time-dependent manner. The microstructural changes of cells in the 5mM, 10 mM, and 20 mM Ca^{2+} groups: abnormal cell morphology, local damage to the cell membrane (red arrow), cell-matrix overflow, free organelles in some areas (green arrow) and many vacuoles (blue arrow) using a transmission electron microscopy (**a**). Pyroptosis- and adhesion-related protein expression in the HK-2 cells using Western Blot images and their graphical quantification (**b**) and ELISA (**c**). $^{*}p<0.05$; $^{**}p<0.01$; $^{***}p<0.001$.

GSDMD expression regulated the adhesion of HK-2 cells

We similarly regulated the level of pyroptosis by knocking down and overexpressing GSDMD to investigate the effect on HK-2 cell adhesion. The qPCR results showed that the mRNA expression levels of the adhesion-related genes OPN, CD44, MCP-1, and ITGB1 were significantly decreased in the sh-GSDMD group and increased in the GSDMD group (Fig. 6a), respectively. The Western blot (Fig. 6b) and ELISA (Fig. 6c) results also showed

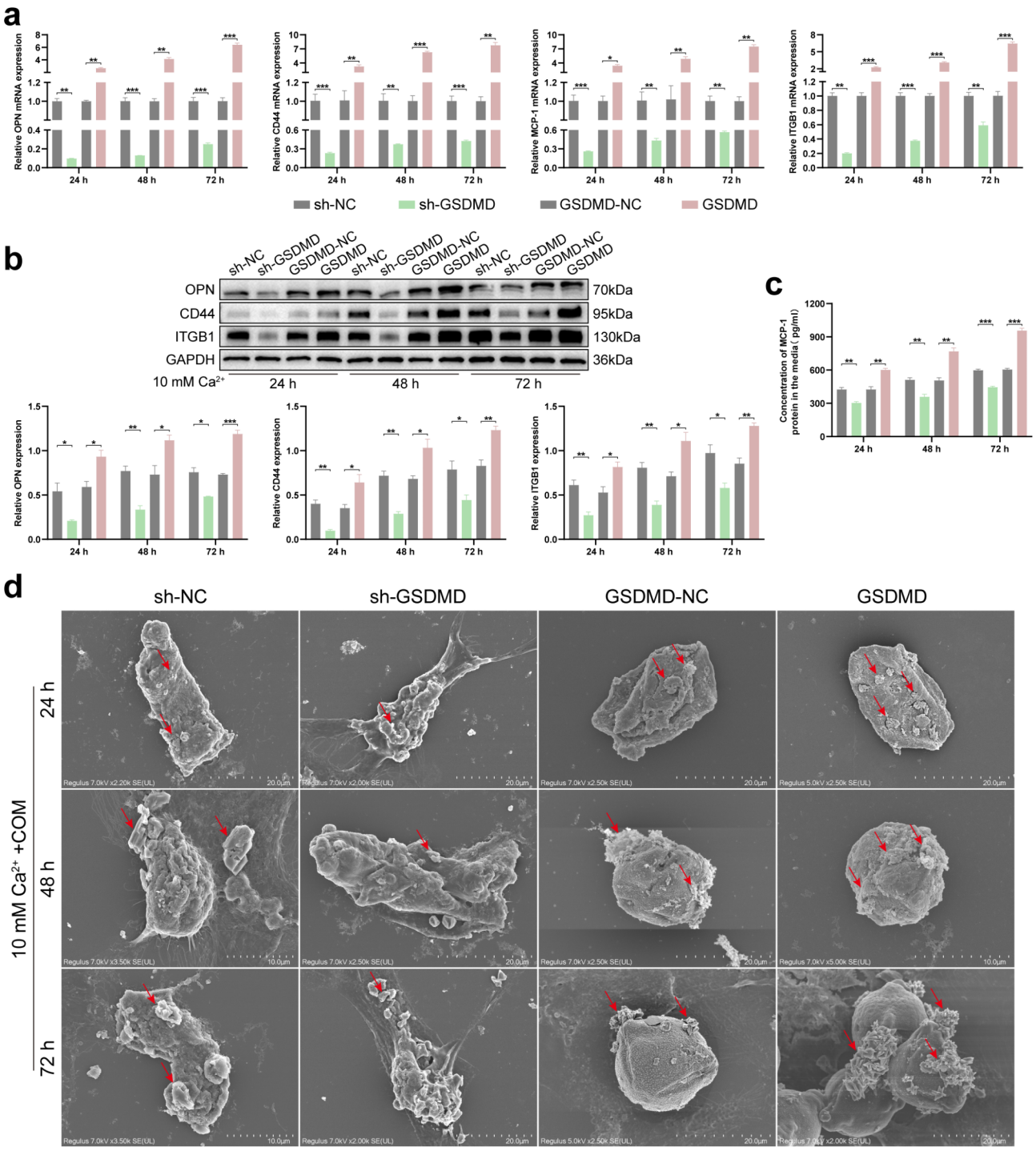

Fig. 6. In vitro: GSDMD regulates the expression of adhesion-related proteins in HK-2 cells. Adhesion-related protein expression in the HK-2 cells using qPCR (**a**), Western Blot images and their graphical quantification (**b**), and ELISA (**c**). The number of adherent crystals (red arrow) on the cell surface of the four groups (sh-NC, sh-GSDMD, GSDMD-NC, and GSDMD) using a scanning electron microscopy (**d**). Significant differences in the GSDMD knockdown and overexpression groups compared to their negative controls. $^{*}p < 0.05$; $^{**}p < 0.01$; $^{***}p < 0.001$.

that the expression levels of these proteins were positively correlated with the expression levels of GSDMD. In addition, the results of scanning electron microscopy (Fig. 6d) also showed that the number of adherent crystals on the surface of the sh-GSDMD group was significantly lower than that on the surface of the sh-NC group when treated with COM and 10 mM Ca^{2+}, while the results were the opposite in the GSDMD group, and the number of adherent crystals on the cell surface was positively correlated with time.

Ca^{2+} treatment promoted the production of ROS in HK-2 cells to activate the NLRP3 inflammasome

Ca^{2+} treatment induced oxidative stress injury in HK-2 cells

HK-2 cells were treated with 5 mM, 10 mM, and 20 mM Ca^{2+} for 24 h. The results of the laser confocal microscopy showed that the level of reactive oxygen species (ROS) in the high Ca^{2+} concentration treatment group was higher than that in the 5 mM Ca^{2+} group (Fig. 7a, b). The results of flow cytometry also showed that the levels of ROS were significantly increased in the 10 mM and 20 mM Ca^{2+} groups compared with the 5 mM Ca^{2+} group (Fig. 7c).

ROS activated NLRP3 inflammasome

The CCK-8 results showed that the cell viability of HK-2 cells decreased after treatment with different concentrations of the ROS inhibitor N-acetylcysteine (NAC) (1.0, 2.5, 5.0, 7.5, 10 mM) for 2 h. The cell viability significantly decreased in the group treated with 7.5 mM NAC compared with that of the control group (Fig. 7d). Therefore, a concentration of 5 mM was used to pretreat the cells for 2 h. Then, the cells were treated with 10 mM Ca^{2+} for 24 h. The Western Blot results showed that compared with the 10 mM Ca^{2+} group, the NAC + 10 mM Ca^{2+} group exhibited significantly decreased expression levels of NLRP3 (Fig. 7e).

High Ca^{2+} up-regulated the level of pyroptosis and adhesion to promote renal tissue damage and calcium oxalate crystal deposition

We established a mouse model of kidney stones and intervened in the urinary calcium concentration in model mice by using potassium citrate (PC). The results of the automatic biochemical analyzer showed that the urinary calcium concentration of the glyoxylic acid (GA) group was significantly higher than that of the Control group, while the urinary calcium concentration of GA + 20% PC group was significantly decreased (Fig. 8a). Subsequently, qPCR (Fig. 8b), Western Blot (Fig. 8c), and immunofluorescence (IF) (Fig. 9) results

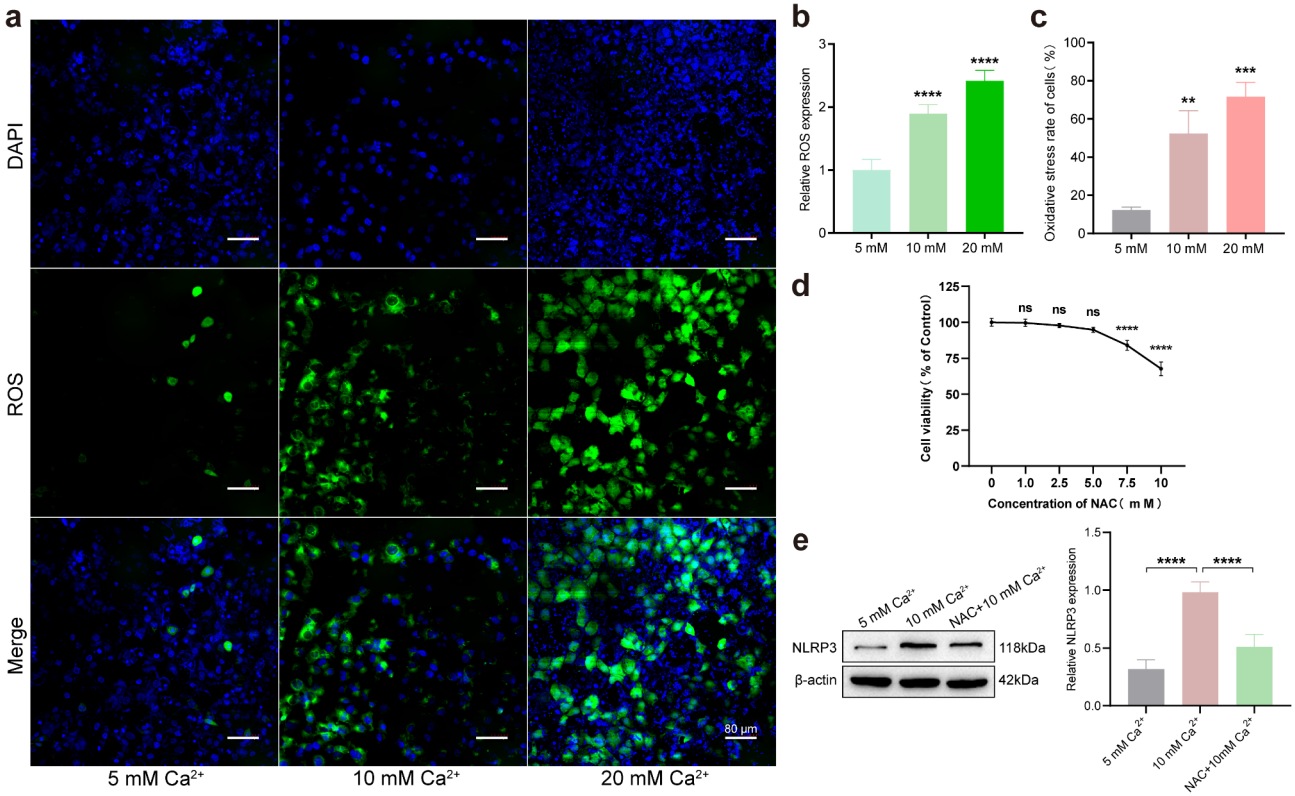

Fig. 7. In vitro: Interconnectivity between oxidative stress and NLRP3 activation in HK-2 cells stimulated with Ca^{2+} (5 mM, 10 mM, and 20 mM [$n = 6$]) at 24 h, and pretreated or not with NAC (5.0 mM [$n = 3$]) at 2 h. Immunofluorescence images (**a**) and their graphical quantification (**b**), flow cytometry (**c**), cell viability (**d**), Western Blot images and their graphical quantification for NLRP3 expression (**e**). $^{**}p < 0.01$; $^{***}p < 0.001$; $^{****}p < 0.0001$.

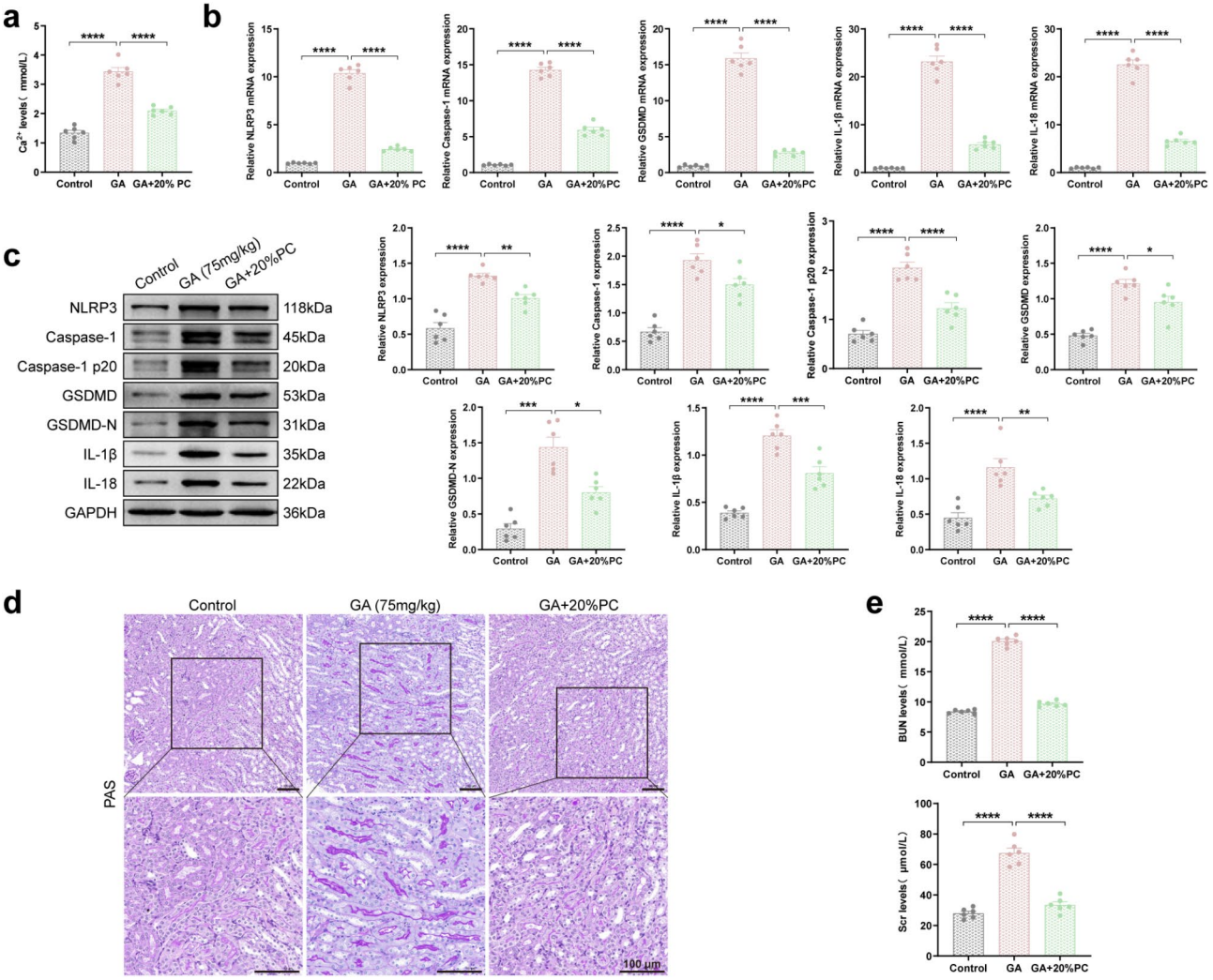

Fig. 8. In vivo: Treatment with potassium citrate (PC). (**a**) 24-hour urinary calcium levels. Pyroptosis-related protein expression in the kidney tissues using qPCR (**b**) and Western Blot images and their graphical quantification (**c**). Periodic acid-Schiff (PAS) staining (**d**), serum creatinine, and blood urea nitrogen levels (**e**). Significant differences in the GA group compared to the Control and GA + 20% PC groups. $^{*}p < 0.05$; $^{**}p < 0.01$; $^{***}p < 0.001$; $^{****}p < 0.0001$.

showed that the expression levels of pyroptosis-related proteins NLRP3, Caspase-1/p20, GSDMD/-N, IL-1β, and IL-18 in the kidney tissues of the GA group were significantly higher than those of the Control group, and compared with the GA group, the expression of related proteins in the kidney tissue of the GA + 20% PC group was significantly down-regulated. We next examined the effect of reducing the urinary calcium concentration on renal function and histologic changes in the mice. Deleterious tissue changes in the medulla (tubular necrosis and casts formation) by periodic acid-Schiff (PAS) staining were more evident in kidneys from the mice in the GA group than Control group and GA + 20% PC group (Fig. 8d). In addition, The results revealed that the mice in GA + 20% PC group have a decrease in blood urea nitrogen (BUN) and serum creatinine (Scr) as compared with the GA group (Fig. 8e).

To confirm the results of Ca^{2+} on the in vitro cell lines at the level of adhesion using an in vivo mouse model, we similarly examined the effect of decreasing urinary calcium concentration on the level of cell adhesion and the development of crystal deposition in mouse renal tissues. qPCR (Fig. 10a), Western Blot (Fig. 10b), and IF (Fig. 11) results showed that the expression levels of adhesion-related proteins OPN, CD44, MCP-1, and ITGB1 in the kidney tissues of the GA group were significantly up-regulated compared with the Control group, and the expression of these proteins in the kidney tissue of the GA + 20% PC group was significantly lower than that of the GA group. Moreover, the development of crystal deposition by Von Kossa staining was less obvious in kidneys from the mice in the GA + 20% PC group than GA group (Fig. 10c).

Together, these results from Figs. 8, 9, 10 and 11 suggest that reducing urinary calcium concentration may lead to a decrease in glyoxylate-induced renal CaOx crystal deposition.

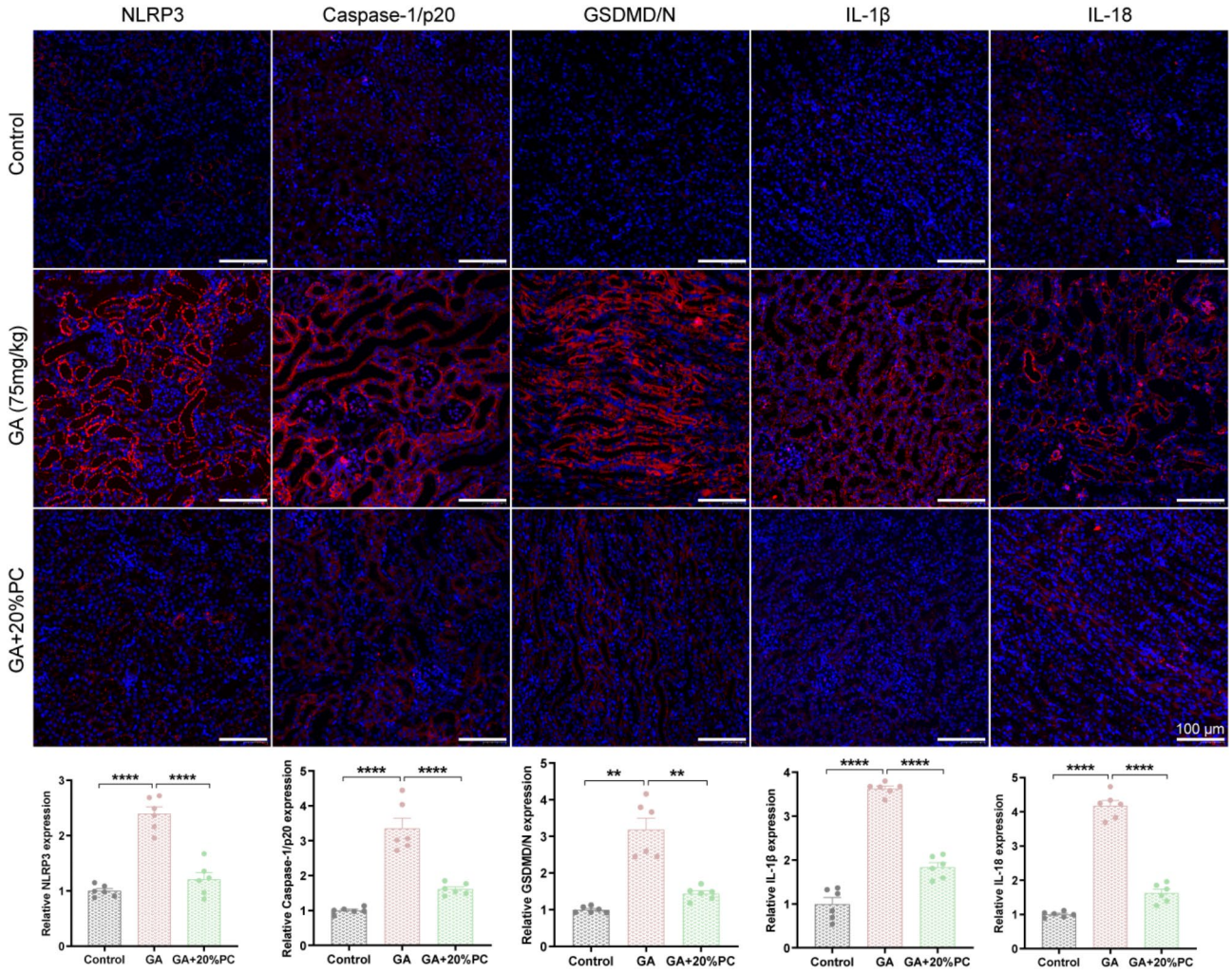

Fig. 9. In vivo: Treatment with potassium citrate (PC). Pyroptosis-related protein expression in the kidney tissues using immunofluorescence images and their graphical quantification. Significant differences in the GA group compared to the Control and GA + 20% PC groups. $^{**}p < 0.01$; $^{****}p < 0.0001$.

Discussion

The exact pathogenesis of kidney stones is still unclear, and its high incidence and recurrence rates greatly affect human life and health, demonstrating the importance of actively studying the mechanism of kidney stones.

Idiopathic hypercalciuria is an important risk factor for the occurrence and development of calcium-containing kidney stones[26]. Ca^{2+} is the cationic component of crystals, and exposure to high concentrations of Ca^{2+} can lead to oxidative stress damage in RTECs[29]. However, CaOx stone formation is associated with oxidative stress damage, increased crystal adhesion, and the inflammatory response that occurs during the pyroptosis of RTECs[19,20,29]. In our in vitro experiments, high Ca^{2+} caused oxidative stress damage to RTECs to generate ROS, which subsequently activated the initiation factor of pyroptosis, the NLRP3 inflammasome. Relevant studies have shown that increased intracellular generation of ROS can cause DNA damage and cell apoptosis[30], activate the NLRP3 inflammasome[31], and result in inflammatory damage to renal tubular epithelial cells[22,32]. Venegas et al.[33] found that pyroptosis and the resulting inflammatory response were significantly reduced when the NLRP3 gene was knocked down or antagonized by an inhibitor, suggesting that NLRP3 is critically involved in pyroptosis. In our study, we identified the promoting role of Ca^{2+} in oxidative stress injury-induced NLRP3 inflammasome activation and pyroptosis in renal tubular epithelial cells. Considering these previous studies, Ca^{2+} might be involved in the pathophysiological process of pyroptosis and the subsequent inflammatory response of RTECs.

CaOx crystals can activate the NADPH oxidase complex to produce ROS through the renin-angiotensin system[21], and increased intracellular generation of ROS can also upregulate the expression of adhesion-associated proteins through the p38 MAPK signaling pathway, which increases cell adhesion to crystals and promotes the attachment of crystals during stone formation[34]. Phosphorylated proteins, such as p38 and c-Jun, play an important role in the regulation of this process[7,35,36]. It has been shown that molecules closely associated with changes in the adhesion of RTECs, OPN, CD44, and MCP-1 are the most widely studied proteins that CaOx crystal attachment depends upon[37–39] and play an important role in the formation of calcium-containing

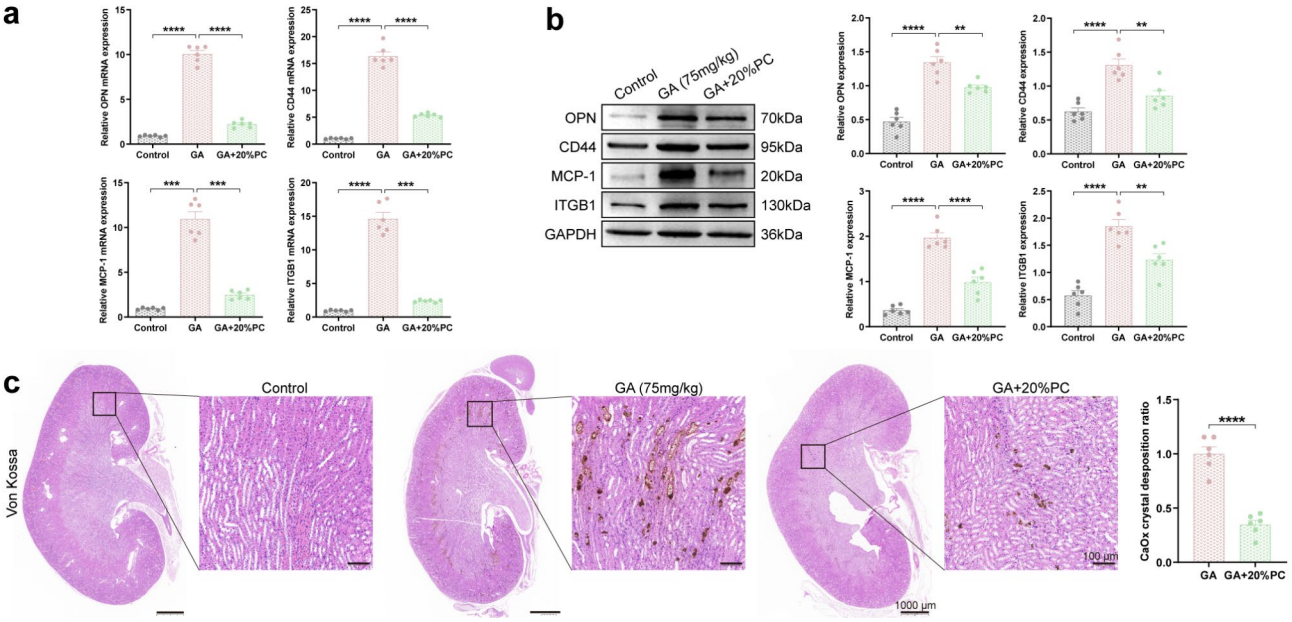

Fig. 10. In vivo: Treatment with potassium citrate (PC). Adhesion-related protein expression in the kidney tissues using qPCR (**a**) and Western Blot images and their graphical quantification (**b**). Von Kossa staining (**c**). Significant differences in the GA group compared to the Control and GA + 20% PC groups. $^{**}p < 0.01$; $^{***}p < 0.001$; $^{****}p < 0.0001$.

kidney stones[40]. ITGB1 is widely expressed in epithelial cells and promotes cell adhesion and growth[41]. In our DEG analysis, the expression of OPN was significantly upregulated in Randall's plaques in patients with kidney stones. We also demonstrated that high Ca^{2+} increased the expression levels of the adhesion-associated proteins, which revealed that Ca^{2+} can increase the adhesion of RTECs.

Bioinformatics analysis showed that the pyroptosis and cell adhesion scores of Randall's plaque tissues were significantly higher than those of normal tissues, and there was a highly positive correlation between these two functions ($R = 0.91$). Relevant studies have found that CaOx crystals exacerbated pyroptosis in HK-2 cells, whereas overexpression of miR-141-3p downregulated pyroptosis-associated proteins to reduce pyroptosis levels, followed by a significant slowing of the rate of kidney stone formation[23]. Joshi et al.[21] also found a significant decrease in the expression levels of renal tubular epithelial cell adhesion-associated proteins OPN, HA, and CD44, as well as a significant reduction in the rate of CaOx stone formation after reducing pyroptosis levels by knocking out the gene NLRP3 in mice. In this study, we regulated the pyroptosis level of renal tubular epithelial cells by knocking down and overexpressing GSDMD, the core pyroptosis-related gene. Our results showed that the expression levels of the adhesion-related proteins were significantly downregulated by GSDMD knockdown and increased by GSDMD overexpression. The results of crystal adhesion experiments similarly demonstrated that the adherent crystals on the cell surface of the renal tubular epithelial cell lines with GSDMD knockdown were significantly reduced and cell damage was significantly attenuated compared to those of the negative control group, whereas the opposite was true for the renal tubular epithelial cells with GSDMD overexpression.

Citrate is readily absorbed in the intestine[42] and decreases calcium absorption and urinary calcium excretion[43,44]. Increased urinary citrate would also bind urinary calcium, removing the calcium from the pool available for binding with phosphate or oxalate. In addition, citrate metabolism to bicarbonate results in systemic alkalinization, which directly decreases bone resorption and increases renal tubule calcium reabsorption, thereby reducing the level of calcium in urine[44,45]. The decrease in urinary calcium by itself would favorably reduce urinary supersaturation for calcium-containing kidney stones. In our in vivo validation experiment, we reduced the urinary calcium concentration in kidney stone model mice by potassium citrate, which resulted in the down-regulation of renal pyroptosis levels and their release of inflammatory factors, improvement of renal injury, and attenuation of renal adhesion levels and deposition of CaOx crystals in response to the reduction in urinary calcium concentration. These results revealed that Ca^{2+} can increase the adhesion of renal tubular epithelial cells by inducing pyroptosis, which results in the aggregation and growth of crystals, and the supersaturation and continuous accumulation of crystals ultimately lead to the formation of kidney stones. However, the limitation of this study was not considered in humans, and further studies should be conducted in clinical CaOx kidney stone formers to support this evidence.

In conclusion, we revealed the mechanism by which the Ca^{2+} and cell adhesion interaction exerts its effect by the NLRP3/Caspase-1/GSDMD classical pyroptosis pathway (Fig. 12). Our study provides new mechanistic insight into the regulatory role of hypercalciuria in CaOx nephrocalcinosis disease and may aid in the development of novel therapeutic strategies targeting Ca^{2+} and pyroptosis-related pathways. Treatments such as reducing urinary Ca^{2+} concentrations or inhibiting the NLRP3 inflammasome pathway may be effective in preventing kidney stones.

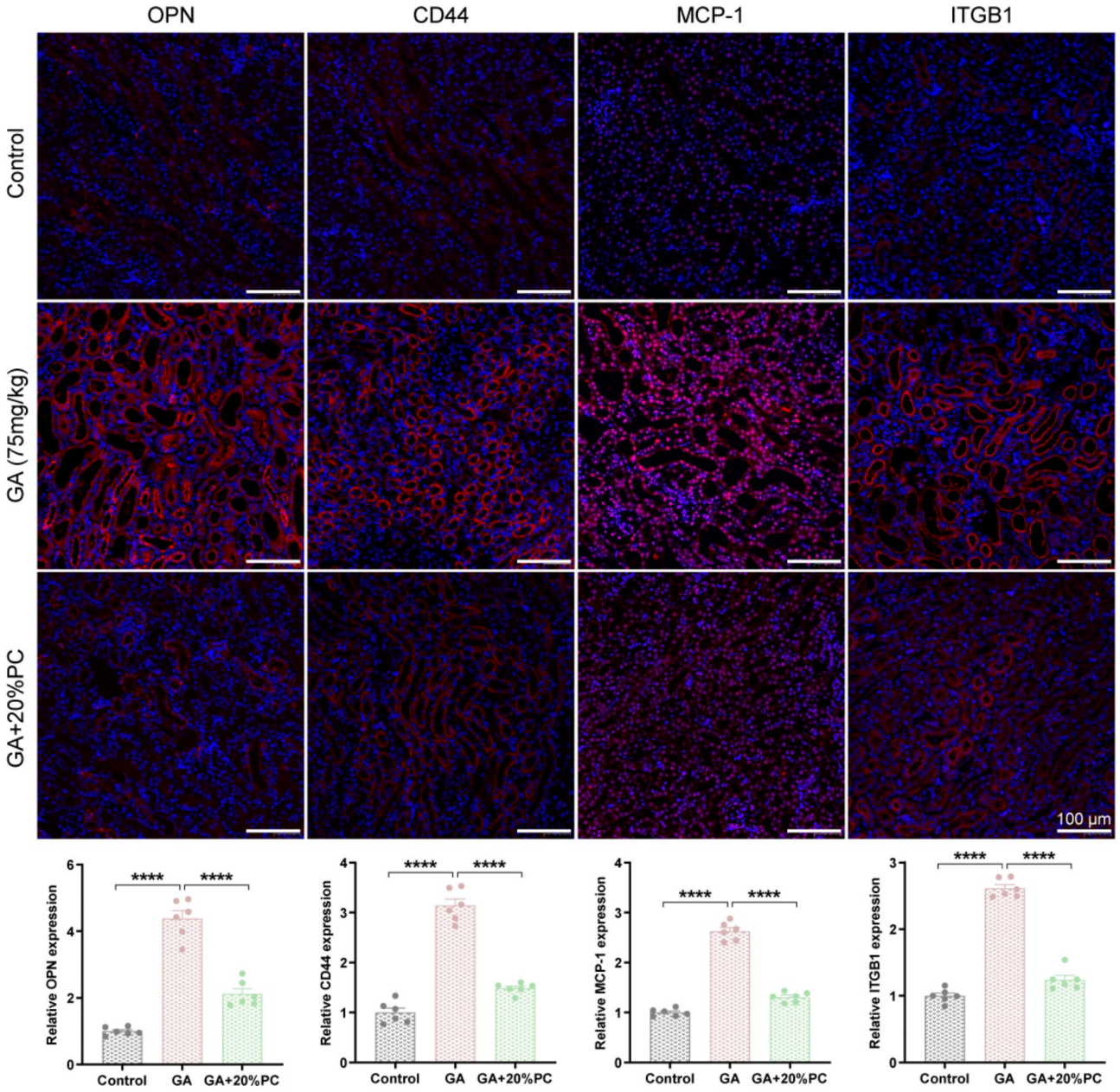

Fig. 11. In vivo: Treatment with potassium citrate (PC). Adhesion -related protein expression in the kidney tissues using immunofluorescence images and their graphical quantification. Significant differences in the GA group compared to the Control and GA + 20% PC groups. ****$p < 0.0001$.

Materials and methods

Bioinformatics analysis

Data obtained and processing

We downloaded the mRNA profiles of the GSE73680 dataset from the public Gene Expression Omnibus (GEO) database managed by the National Center for Biotechnology Information- NCBI (Bethesda, EUA). GSE73680 contained 29 CaOx stone patients and 6 healthy controls. We performed differential gene screening and functional enrichment analysis to compare the DEGs related to the function of renal tubular epithelial cells in Randall's plaques and normal tissue from calcium stone patients, analyzed the coexpressed gene modules related to pyroptosis and cell adhesion by weighted gene coexpression network analysis (WGCNA), and calculated the pyroptosis score and cell adhesion score by single-sample GSEA using the GSVA package in R. Group P: Randall's plaque tissues from calcium stone patients ($n = 29$), Group N: normal tissues from calcium stone patients ($n = 27$), and Group C: normal tissues from healthy controls ($n = 6$).

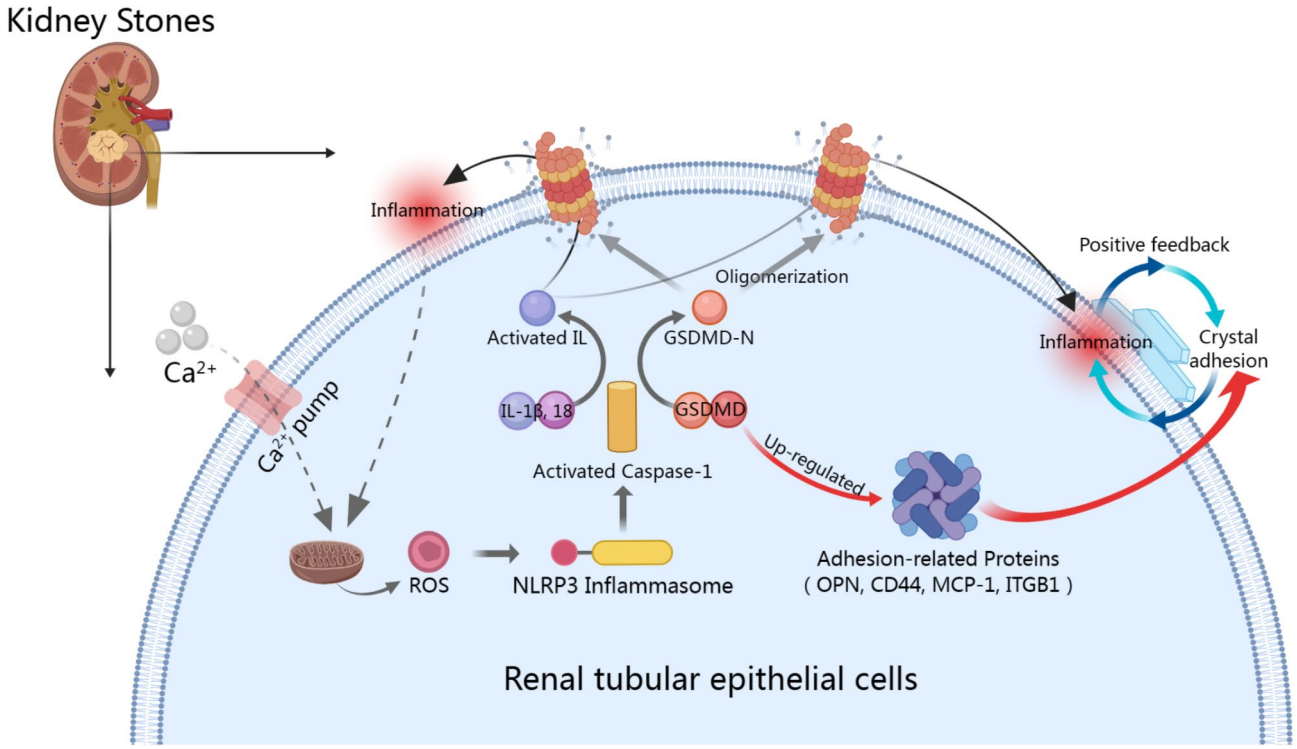

Fig. 12. A schematic diagram for the underlying mechanism of the Ca^{2+} in regulating calcium oxalate stone formation. High concentrations of Ca^{2+} activates the NLRP3/Caspase-1/GSDMD pathway of pyroptosis through ROS and up-regulated the expression of adhesion-related proteins, thereby affecting the adhesion and deposition of crystals, and eventually leads to the formation of calcium oxalate kidney stones.

Screening DEGs and biological function analysis

The GSE73680 expression matrices were log2 transformed and normalized by the R function "normalizeBetweenArrays". Based on the cutoff value of p-value < 0.05 and the absolute log2 |fold change (log2FC)| > 0.5, GSE73680 successfully adopted the LIMMA package to select DEGs. Then, GO and KEGG analysis were used to rank gene functions and pathways by applying the "clusterProfiler" R package[46].

GSEA

GSEA was performed to identify the most significantly enriched pathways between group P and group N using the clusterProfiler package in R.

Weight gene co-expression network analysis (WGCNA)

WGCNA is an analysis method to analyze the gene expression patterns of multiple samples, which can cluster genes with similar expression patterns and analyze the association between modules and specific traits or phenotypes. In this study, to identify the genes associated with different traits, WGCNA was performed on the GSE73680 dataset, and kidney stones, pyroptosis, cell adhesion, and Ca^{2+} pathways were analyzed as traits by WGCNA.

The specific steps of the analysis were as follows: (1) Sample clustering to check the overall correlation of all samples in the dataset. We first clustered the samples and removed outlier samples to ensure the accuracy of the analysis. (2) Constructing sample clusters and clinical traits. (3) Soft threshold determination. A rational soft power threshold was recommended for the adjacency matrix through the "pickSoftThreshold" function built into the "WGCNA" package from 1 to 20. (4) Construction of coexpression networks. Genes with similar expression profiles could be attributed to various gene modules by employing the dynamic tree-cutting function. We set the module's correlation coefficient threshold and merged homologous modules in a dynamic cluster tree. (5) Correlation analysis of modules and clinical characteristics. The following procedure evaluates the expression-trait correlation plotted in various random color modules. The highest correlated module eigengene (ME) was identified as the key gene group with gene significance (GS) $p < 0.05$. (6) Screening of Ca^{2+} pathway modules. (7) Correlation analysis between modules and pyroptosis. We used the GSVA R package and pyroptosis gene set to perform a single-sample enrichment analysis of each sample to evaluate the correlation between pyroptosis and the modules.

Cell culture

The normal human proximal tubular epithelial cell line HK-2 was kindly provided by Procell Life Science & Technology Co., Ltd. (Wuhan, China) and maintained in Dulbecco's modified Eagle's medium and F12 medium

(DMEM/F12) supplemented with 10% fetal bovine serum (ExCell, Shanghai, China) and 1% penicillin/streptomycin in a humidified atmosphere of 5% CO2.

All experiments were repeated multiple times at different times and the sampling is sufficient to ensure statistically significant results.

Cell viability assay

Five 96-well plates were used to culture HK-2 cells at different times. Cells were incubated with 100 μL of culture medium containing different concentrations (1, 5, 10, 20, 30, 40 mM [$n = 5$]) of $CaCl_2$ (Yuanye, Shanghai, China) for 24 h, 48 h, and 72 h to release Ca^{2+} ions and induce hypercalciuria, and different concentrations (1.0, 2.5, 5.0, 7.5, 10 mM [$n = 5$]) of NAC (Proteintech, USA) for 2 h. Subsequently, 10 μL CCK-8 reagent (Proteintech, USA) was added to each well and incubated in a constant-temperature incubator at 37 °C for 2 h. The optical density (OD) was read at 450 nm on a microplate reader and the results were expressed as a line chart. We used a concentration of Ca^{2+} that significantly reduced the viability of HK-2 cells but not less than 50% for subsequent experiments.

LDH release

Media were aliquoted into selected wells of the 96-well plate. A LDH assay kit (Nanjing Jiancheng, China) was used to determine the percent LDH release. The substrate and chromophoric reagent supplied with the kit were added to the blanks (acclimatization media), positive control, and all samples. The plate was incubated for 15 min at 37 ℃. The stop solution, supplied with a kit, was added to all of the wells, and the plate was incubated for 3 min at room temperature. A microplate reader was used to read the OD at 440 nm and the results were expressed as a line chart. We used a concentration of Ca^{2+} that did not cause damage to HK-2 cells for subsequent experiments.

Reagents and transfection

To knock down and overexpress of GSDMD, lentivirus GSDMD and a negative control were synthesized by Generalbiol (Anhui, China) and purchased. Lentivirus was diluted with 500 μL of Opti-MEM medium at 10^8 transduction units (TU)/mL containing polybrene (5 mg/mL) and incubated with cells for 12 h. The medium was then replaced with DMEM/F12 and cultured for 24 h. Then, subsequent screening with puromycin yielded stably transfected cell lines. Sh-NC (HK-2 cells transfected with blank silencing lentivirus, $n = 3$), Sh-GSDMD (HK-2 cells with silenced GSDMD expression, $n = 3$), GSDMD-NC (HK-2 cells transfected with blank overexpressing lentivirus, $n = 3$), GSDMD (HK-2 cells with overexpressed GSDMD expression, $n = 3$). These groups were concomitantly stimulated with calcium oxalate monohydrate (COM-100 μg/mL) and Ca^{2+} (10 mM) for 24 h, 48 h, and 72 h.

Animal procedures

All experimental procedures were in accordance with the regulations on the management of experimental animals of Kunming Medical University and approved by the Animal Ethics Committee. C57BL/6 N male mice (6–8 weeks old) were used in the experiments. To establish the CaOx nephrocalcinosis model, each C57BL/6 N male mouse received either intraperitoneal saline or GA (75 mg/kg, 200 μL) every day for two weeks[47]. In the Ca^{2+} intervention groups, PC was used to reduce urinary calcium concentration in mice[44], and each mouse was gavaged with 20% PC (2 g/kg, 200 μL) solution daily for two weeks while the other groups were gavaged with an equal amount of saline. So the mice were divided into three groups: Control group (gavaged with saline and received intraperitoneal saline, $n = 6$), GA group (gavaged with saline and received intraperitoneal GA, $n = 6$), and GA + 20% PC group (gavaged with 20% PC and received intraperitoneal GA, $n = 6$). After two weeks, 24-h urine was collected from each group of mice using metabolic cages, and blood was collected by enucleation of eyeballs, and then the mice were euthanized by a physical method (cervical dislocation), and the kidneys were removed by laparotomy for further assessment. Urine and blood were analyzed by an automatic biochemical analyzer and kidney tissue sections were stained with periodic acid-Schiff (PAS) and Von Kossa to assess tubular injury and crystal formation/adhesion, and then quantified as the percent area of crystal deposition per kidney section with Image-Pro-Plus.

Observation of cellular microstructural changes

HK-2 cells were harvested with Ca^{2+} (5 mM, 10 mM, and 20 mM [$n = 3$]) for 24 h, 48 h, and 72 h. Cell clusters were fixed by the addition of 2.5% glutaraldehyde and wrapped using 1% agarose, followed by dehydration, embedding, sectioning, double staining with uranium-lead, and drying overnight, and images were acquired and analyzed by using a transmission electron microscopy (FEI Tecnai G2 Spirit, USA). The results were expressed as original images.

RNA extraction and qPCR

Total RNA was extracted from the control and experimental groups using a total RNA extraction kit (TIANGEN, China) and then reverse transcribed using a reverse transcription kit (Vazyme, China). qPCRs were conducted on an Applied Biosystems 7500 system with ChamQ Universal SYBR qPCR Master Mix (Vazyme, China). All amplifications were followed by a dissociation curve analysis of the amplified products. Relative RNA expression of the gene was calculated using the $2^{(-\Delta\Delta Ct)}$ method and normalized to GAPDH expression[47]. The results were expressed as a histogram. Specific primers were designed using NCBI and the sequence identity was confirmed with BLAST. The primers used in our research are presented in Supplementary Table 1.

Western blot
Protein extracts were separated by SDS-PAGE, transferred to PVDF membranes, and incubated overnight at 4 °C with primary antibodies. Then, the membrane strips were incubated with the appropriate horseradish peroxidase-conjugated secondary antibodies. The protein bands were visualized using an ECL kit (Proteintech, USA), and ImageJ software was used to calculate the relative density of proteins. The results were expressed as a histogram.

ELISA
The cells were treated with Ca^{2+} (5 mM, 10 mM, and 20 mM [$n = 3$]) for 24 h, 48 h, and 72 h, the culture medium was collected and centrifuged to obtain the supernatant, and the levels of the pyroptosis-related inflammatory factors IL-1β and IL-18, and the adhesion-related MCP-1 in the culture supernatant were measured by using an ELISA kit (Proteintech, USA). The results were expressed as a histogram.

Histology and immunofluorescence
Kidneys from mice were fixed for 72 h with 4% buffered polyformaldehyde before embedding in paraffin. Serial sections at 5 μm thick were obtained for histologic analysis. Hematoxylin and eosin (H&E) staining involved standard procedures.

For IF, sections were incubated with the primary antibodies. To enhance antigen exposure, the sections were treated with 10 mM sodium citrate/pH 6.0 at 98 °C for 15 min for antigen retrieval. The sections were incubated with 3% BSA blocking solution, and then were incubated with the primary antibody at 4 ℃ overnight. After rinsing with PBS, the sections were incubated for 50 min with secondary antibody, washed, and then incubated with DAPI staining solution for 10 min. After rinsing again, the tissue autofluorescence was quenched using an autofluorescence quencher, and the sections were sealed using an anti-fluorescence quenching sealer, and finally the sections were observed using a fluorescence microscope (Nikon ECLIPSE C1, Japan) and images were captured (Nikon DS-U3, Japan). The results were expressed as original images.

Antibodies
The antibodies used in this study are listed in Supplementary Table 2.

COM crystals preparation and crystal adhesion analysis
Calcium oxalate monohydrate (COM) crystals were prepared as described previously[48]. Cells were seeded in round coverslips and incubated in a culture medium containing 100 μg/mL COM[37] and 10 mM Ca^{2+} for 24 h, 48 h, and 72 h. Cells were washed 3 times with PBS, fixed with 2.5% glutaraldehyde at 4 °C in the dark. Then, they were subsequently washed, dehydrated, dried at the critical point, and metal-coated to observe crystal adhesion on the cell surface under scanning electron microscopy (Hitachi SU8100, Japan).

ROS assay and effects on the NLRP3 inflammasome
HK-2 cells were cultured in a laser confocal dish and 6-well plates, and exposed to Ca^{2+} (5 mM, 10 mM, and 20 mM, [$n = 6$]) for 24 h. Then, the cells were treated with 2,7-dichlorofluorescein diacetate (DCFH-DA)[49] for 30 min, and the intracellular ROS levels were observed by laser scanning confocal microscopy (LSCM). The cells in the 6-well plates were collected and resuspended in PBS, and intracellular ROS production was determined using flow cytometry with excitation and emission at 488 and 525 nm, respectively.

The cells were pretreated with the ROS inhibitor NAC (5 mM, [$n = 3$]) for 2 h. Subsequently, each group of cells was incubated with 10 mM Ca^{2+} for 24 h. Western blot was used to detect the expression level of the NLRP3 inflammasome proteins in the cells. ImageJ software was used to calculate the relative density of ROS and proteins.

Data analysis
GraphPad Prism 9.4 and SPSS 26.0 software were used for statistical analysis, and quantitative data were normally distributed and analyzed by a two-tailed *t*-test or one-way ANOVA. The results are expressed as the mean ± SEM. $p < 0.05$ for the difference was defined as statistically significant.

Data availability
The data that support the findings of this study are available from the corresponding author upon reasonable request.

Received: 16 May 2024; Accepted: 20 February 2025
Published online: 24 February 2025

References
1. Thongprayoon, C., Krambeck, A. E. & Rule, A. D. Determining the true burden of kidney stone disease. *Nat. Rev. Nephrol.* **16**, 736–746 (2020).
2. Du, Y. et al. Structural and chemical heterogeneities of primary hyperoxaluria kidney stones from pediatric patients. *J. Pediatr. Urol.* **17**, 214e1–214e11 (2021).
3. Liu, B. C., Tang, T. T., Lv, L. L. & Lan, H. Y. Renal tubule injury: A driving force toward chronic kidney disease. *Kidney Int.* **93**, 568–579 (2018).
4. Honarpisheh, M. et al. Phagocytosis of environmental or metabolic crystalline particles induces cytotoxicity by triggering necroptosis across a broad range of particle size and shape. *Sci. Rep.* **7**, 15523 (2017).
5. Khan, S. R. Reactive oxygen species, inflammation and calcium oxalate nephrolithiasis. *Transl Androl. Urol.* **3**, 256–276 (2014).

6. Khan, S. R. Crystal-induced inflammation of the kidneys: Results from human studies, animal models, and tissue-culture studies. *Clin. Exp. Nephrol.* **8**, 75–88 (2004).
7. Liu, Q. et al. Effect of M2 macrophages on injury and apoptosis of renal tubular epithelial cells induced by calcium oxalate crystals. *Kidney Blood Press. Res.* **44**, 777–791 (2019).
8. Randall, A., The origin and & growth of renal calculi. *Ann. Surg.* **105**, 1009–1027 (1937).
9. Coe, F. L., Evan, A. P., Lingeman, J. E. & Worcester, E. M. Plaque and deposits in nine human stone diseases. *Urol. Res.* **38**, 239–247 (2010).
10. Evan, A. P. Physiopathology and etiology of stone formation in the kidney and the urinary tract. *Pediatr. Nephrol.* **25**, 831–841 (2010).
11. Fang, Y. et al. Pyroptosis: A new frontier in cancer. *Biomed. Pharmacother.* **121**, 109595 (2020).
12. Frank, D. & Vince, J. E. Pyroptosis versus necroptosis: Similarities, differences, and crosstalk. *Cell. Death Differ.* **26**, 99–114 (2019).
13. Hutton, H. L., Ooi, J. D., Holdsworth, S. R. & Kitching, A. R. The NLRP3 inflammasome in kidney disease and autoimmunity. *Nephrol. (Carlton).* **21**, 736–744 (2016).
14. Li, X. et al. Long noncoding RNA MALAT1 regulates renal tubular epithelial pyroptosis by modulated miR-23c targeting of ELAVL1 in diabetic nephropathy. *Exp. Cell. Res.* **350**, 327–335 (2017).
15. Vilaysane, A. et al. The NLRP3 inflammasome promotes renal inflammation and contributes to CKD. *J. Am. Soc. Nephrol.* **21**, 1732–1744 (2010).
16. Xu, G. et al. Defects in MAP1S-mediated autophagy turnover of fibronectin cause renal fibrosis. *Aging (Albany N Y).* **8**, 977–985 (2016).
17. Hou, J. et al. PD-L1-mediated gasdermin C expression switches apoptosis to pyroptosis in cancer cells and facilitates tumour necrosis. *Nat. Cell. Biol.* **22**, 1264–1275 (2020).
18. Ma, Y., Chen, Y., Lin, C. & Hu, G. Biological functions and clinical significance of the newly identified long non–coding RNA RP1–85F18.6 in colorectal cancer. *Oncol. Rep.* **40**, 2648–2658 (2018).
19. Anders, H. J. et al. The macrophage phenotype and inflammasome component NLRP3 contributes to nephrocalcinosis-related chronic kidney disease independent from IL-1-mediated tissue injury. *Kidney Int.* **93**, 656–669 (2018).
20. Khan, S. R., Canales, B. K. & Dominguez-Gutierrez, P. R. Randall's plaque and calcium oxalate stone formation: Role for immunity and inflammation. *Nat. Rev. Nephrol.* **17**, 417–433 (2021).
21. Joshi, S., Wang, W., Peck, A. B. & Khan, S. R. Activation of the NLRP3 inflammasome in association with calcium oxalate crystal induced reactive oxygen species in kidneys. *J. Urol.* **193**, 1684–1691 (2015).
22. Lin, Q. et al. PINK1-parkin pathway of mitophagy protects against contrast-induced acute kidney injury via decreasing mitochondrial ROS and NLRP3 inflammasome activation. *Redox Biol.* **26**, 101254 (2019).
23. Gan, X. G., Wang, Z. H. & Xu, H. T. Mechanism of miRNA-141-3p in calcium Oxalate-Induced renal tubular epithelial cell injury via NLRP3-Mediated pyroptosis. *Kidney Blood Press. Res.* **47**, 300–308 (2022).
24. Ding, T. et al. Vitexin exerts protective effects against calcium oxalate crystal-induced kidney pyroptosis in vivo and in vitro. *Phytomedicine* **86**, 153562 (2021).
25. Worcester, E. M. & Coe, F. L. New insights into the pathogenesis of idiopathic hypercalciuria. *Semin Nephrol.* **28**, 120–132 (2008).
26. Coe, F. L., Worcester, E. M. & Evan, A. P. Idiopathic hypercalciuria and formation of calcium renal stones. *Nat. Rev. Nephrol.* **12**, 519–533 (2016).
27. Wang, Y. et al. Urinary MCP-1、HMGB1 increased in calcium nephrolithiasis patients and the influence of hypercalciuria on the production of the two cytokines. *Urolithiasis* **45**, 159–175 (2017).
28. Daudon, M., Hennequin, C., Boujelben, G., Lacour, B. & Jungers, P. Serial crystalluria determination and the risk of recurrence in calcium stone formers. *Kidney Int.* **67**, 1934–1943 (2005).
29. Khaskhali, M. H., Byer, K. J. & Khan, S. R. The effect of calcium on calcium oxalate monohydrate crystal-induced renal epithelial injury. *Urol. Res.* **37**, 1–6 (2009).
30. Yan, Q. et al. Effects of alternative splicing events and transcriptome changes on kidney stone formation. *Urolithiasis* **50**, 131–140 (2022).
31. Yu, X. et al. HBV inhibits LPS-induced NLRP3 inflammasome activation and IL-1β production via suppressing the NF-κB pathway and ROS production. *J. Hepatol.* **66**, 693–702 (2017).
32. Han, Y. et al. Reactive oxygen species promote tubular injury in diabetic nephropathy: The role of the mitochondrial ros-txnip-nlrp3 biological axis. *Redox Biol.* **16**, 32–46 (2018).
33. Venegas, C. & Heneka, M. T. Inflammasome-mediated innate immunity in Alzheimer's disease. *FASEB J.* **33**, 13075–13084 (2019).
34. Peerapen, P. & Thongboonkerd, V. p38 MAPK mediates calcium oxalate crystal-induced tight junction disruption in distal renal tubular epithelial cells. *Sci. Rep.* **3**, 1041 (2013).
35. Qi, S. et al. P38 MAPK signaling pathway mediates COM crystal-induced crystal adhesion change in rat renal tubular epithelial cells. *Urolithiasis* **48**, 9–18 (2020).
36. Khan, S. R. Role of renal epithelial cells in the initiation of calcium oxalate stones. *Nephron Exp. Nephrol.* **98**, e55–60 (2004).
37. Wang, Z. et al. Comprehensive study of altered proteomic landscape in proximal renal tubular epithelial cells in response to calcium oxalate monohydrate crystals. *BMC Urol.* **20**, 136 (2020).
38. Asselman, M., Verhulst, A., De Broe, M. E. & Verkoelen, C. F. Calcium oxalate crystal adherence to hyaluronan-, osteopontin-, and CD44-expressing injured/regenerating tubular epithelial cells in rat kidneys. *J. Am. Soc. Nephrol.* **14**, 3155–3166 (2003).
39. Qin, B. et al. Losartan Ameliorates Calcium Oxalate-Induced Elevation of Stone-Related Proteins in Renal Tubular Cells by Inhibiting NADPH Oxidase and Oxidative Stress. *Oxid. Med. Cell. Longev.* **1271864** (2018). (2018).
40. Khan, S. R. Calcium oxalate crystal interaction with renal tubular epithelium, mechanism of crystal adhesion and its impact on stone development. *Urol. Res.* **23**, 71–79 (1995).
41. Damanakis, A. I. et al. Integrin beta1 (ITGB1) as a prognostic marker in esophageal adenocarcinoma. *Sci. Rep.* **12**, 20745 (2022).
42. Fegan, J., Khan, R., Poindexter, J. & Pak, C. Y. Gastrointestinal citrate absorption in nephrolithiasis. *J. Urol.* **147**, 1212–1214 (1992).
43. Rümenapf, G. & Schwille, P. O. The influence of oral alkali citrate on intestinal calcium absorption in healthy man. *Clin. Sci.* **73**, 117–121 (1987).
44. Krieger, N. S. et al. Effect of potassium citrate on calcium phosphate stones in a model of hypercalciuria. *J. Am. Soc. Nephrol.* **26**, 3001–3008 (2015).
45. Bushinsky, D. A. Metabolic alkalosis decreases bone calcium efflux by suppressing osteoclasts and stimulating osteoblasts. *Am. J. Physiol.* **271**, F216–F222 (1996).
46. Yu, G., Wang, L. G., Han, Y. & He, Q. Y. ClusterProfiler: an R package for comparing biological themes among gene clusters. *OMICS* **16**, 284–287 (2012).
47. Liu, H. et al. H19 promote calcium oxalate nephrocalcinosis-induced renal tubular epithelial cell injury via a CeRNA pathway. *EBioMedicine* **50**, 366–378 (2019).
48. Zhu, W. et al. Loss of the androgen receptor suppresses intrarenal calcium oxalate crystals deposition via altering macrophage recruitment/M2 polarization with change of the miR-185-5p/CSF-1 signals. *Cell. Death Dis.* **10**, 275 (2019).
49. Rizvi, S. H. M. et al. Aluminum activates PERK-EIF2α signaling and inflammatory proteins in human neuroblastoma SH-SY5Y cells. *Biol. Trace Elem. Res.* **172**, 108–119 (2016).

Acknowledgements
We express our gratitude to all the authors who have contributed to this research topic.

Author contributions
J.X. and H.L. designed the study. J.X. was responsible for the writing and critical revisions of the manuscript. In vitro experiments were implemented by J.X., M.L., and Y.L. J.X., K.K., and B.Z. performed in vivo experiments. Data collection and analysis were performed by M.W. and K.Z. H.L. contributed to the interpretation of the results during all phases and edited the final manuscript. All authors have read and approved the final manuscript.

Funding
This work was supported by the Yunnan Province Science and Technology Department (202001AY070001-158) and Yunnan Revitalization Talent Support Program.

Declarations

Competing interests
The authors declare no competing interests.

Ethics approval and consent to participate
The study was supervised and approved by the Ethics Committee of Kunming Medical University (Approval number: kmmu20220691), and reported in accordance with ARRIVE guidelines. All protocols were performed according to the Declaration of Helsinki.

Additional information
Supplementary Information The online version contains supplementary material available at https://doi.org/10.1038/s41598-025-91460-8.

Correspondence and requests for materials should be addressed to H.L.

Reprints and permissions information is available at www.nature.com/reprints.

Publisher's note Springer Nature remains neutral with regard to jurisdictional claims in published maps and institutional affiliations.